Absorption features of high-redshift galactic winds

A.P.M. Fangano, A. Ferrara, P. Richter*

Argelander-Institut für Astronomie

universitätbonn

Introduction

A major problem in our current understanding of the InterGalactic Medium (IGM) is to determine when and by what transport means metals have been transported from galaxies to it. One possible mechanism is based on the idea that the energy/momentum deposited by multiple supernovae can drive an outflow of material from the host galaxy to the surrounding IGM. Yet, the epoch when most of the enrichment took place is still unclear. With the combined analysis of quasars (QSOs) and galaxy spectra it is possible to connect the properties of the intergalactic absorption lines with that of the foreground galaxies. For this aim, simulations can be quite helpful. In the framework of these recent studies we have analyzed outputs from a GADGET cosmological simulation that uses state-of-art treatment of multiphase ISM, winds and metal pollution with the intent of providing quantitative and clear-cut diagnostics for observational investigation of outflow phenomena around high redshift galaxies.

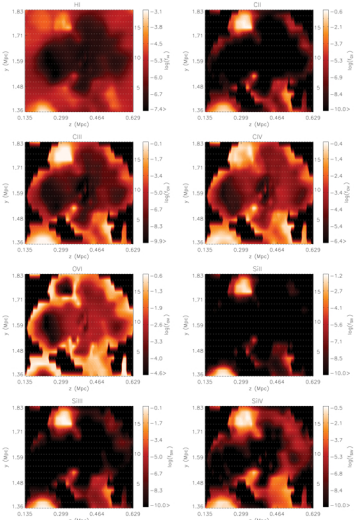

Figure 3. Ionization fraction maps across the target galaxy center for various ions are shown. The dotted lines indicate the analyzed line of sight (LOS) numbered from 1 to 18 as labeled to the right of each panel.

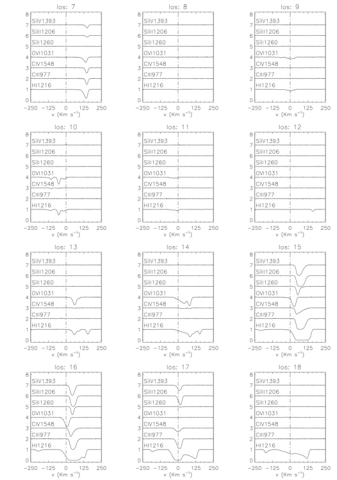

Figure 4. Absorption systems for the LOS #7-18 (labeled at the top of each panel) through the wind bubble; see Fig.1 for their positions and ionization conditions. Negative (positive) velocities denote approaching (receding) flows with respect to the observer.

Wind environment tracers

To analyze the sub-volume containing the selected galaxy, we have drawn 1600 LOSs through it. The ionization equilibrium, under the influence of the UV background adopted in the simulation, has been calculated in each of the (~ 100) cells into which each LOS has been segmented, using the code CLOUDY96. As seen from Fig. 3, in which we show the spatial distribution of the ionization fractions of various ions, the bubble interior is characterized by a very low abundance of most of the species shown, with the only significant exception of OVI. This appears to be almost homogeneously distributed in the volume, with drops in abundance in isolated regions (infalling cold clumps). In addition to OVI the bubble region is characterized by considerable abundances of OVII and OVIII. These ions would then represent very reliable tracers of active outflow regions. The cooler gas phases (i.e. clump in the upper left region of the maps) are instead best traced by low-ionization species such as CII, CIII, SiII, and SiIII. Intermediate ionization ions (CIV and SiIV) are typically found in the interfaces between the cooler and the hot gas phase. It is worth noticing that CIV extends deeper into the bubble region than SiIV. A first qualitative conclusion drawn from the maps is then that the bubbles could be identified by searching for absorbers that simultaneously have low SiIV/CIV ($\log(f_{SiIV}/f_{CIV}) < -2$) and very high OVI/CIV ($\log(f_{OVI}/f_{CIV}) > 1$) ratios. Typical examples for this behavior are seen in the spectra obtained from LOS #10 and #14 shown in Fig. 4, where we present a selection of absorption spectra along the LOSs defined in Fig. 3. Both LOSs exhibit strong OVI and weak CIV absorption systems caused by infalling (v > 0) material, but no SiIV is detected. Only sightlines piercing regions of enhanced density (e.g. LOS #14) and/or located nearby the target galaxy (LOS #10) exhibit clear signs of CIV absorption. The cold clump itself instead is characterized by the presence of SiII, SiIII and SiIV (LOS #15, #16 and #17). It appears that the volume occupied by a given element (here Si) increases with its ionization state; the same conclusion holds for carbon ions.

Numerical Simulations

Our analysis is based on a hydrodynamic cosmological simulation that adopts a ΛCDM cosmological model with Ω_M=0.3, Ω_Λ=0.7, Ω_b=0.04, h=0.7, σ_8=0.8 and periodic boundary conditions. The numerical code used for the simulation is a modified version of GADGET (Marri & White (2003)); in brief additions concern: (i) an improved treatment of the multiphase nature of the gas, and (ii) a more refined recipe for stellar feedback. The scheme also tracks the gas metal enrichment due to supernova (SN) explosions. This allows us to apply the so-called *critical metallicity* criterion introduced by Schneider et al. (2002) according to which, the Initial Mass Function (IMF) of star forming sites is biased towards very massive (PopIII) stars if the metallicity is below $Z_{cr}=10^{-4}\,Z_\odot$; otherwise a classical Salpeter IMF occurs (PopII stars). These stellar populations have distinct feedback prescriptions, depending on the explosion energies and metal production efficiencies of PopIII and PopII stars.We have run simulations at two different resolutions. The low resolution simulation consists of 64^3 particles simulating a 7.0 h^{-1} comoving Mpc; the high resolution run is made up of 128^3 particles in a 10.5 h^{-1} comoving Mpc. Both have a mass resolution of M ~ 10^6 $M_\odot$ h^{-1}. In both runs the evolution was followed including the effect of a UV-background taken from Haardt & Madau (2001). In Tab. 1 and Fig. 1 we show a comparison with observations of the metal content of the low resolution run. Unless otherwise specified we report results based on the high resolution run.

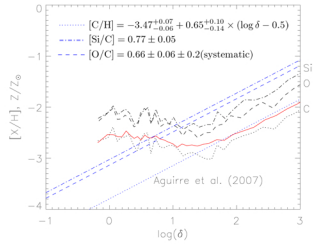

Figure 1. Abundances relative to solar for C (dotted), O (dashed) and Si (dot-dashed) as a function of overdensity. The thick red curve represents the values for the total metallicity relative to solar while the blue lines show the relation found by Aguirre et al. 2007 for [C/H] , [Si/H] and [O/H].

Element	Tracer	Abundances	
$[C/H]$	CIV	−2.58	$-2.82^1, -3.47^2$
$[O/H]$	OVI	−2.14	$-2.82^1, [-2.22, -1.3]^3$
$[Si/H]$	SiIV	−1.99	-2.00^4

[1] Schaye et al. (2003), [2] Simcoe et al. (2004)
[3] Telfer et al. (2002), [4] Aguirre et al. (2004)

Table 1. Abundances values relative to solar from our low resolution run: shown are the considered element (first column), transition used as tracer (second), median value retrieved from our simulation (third), observed values (forth). For a meaningful comparison with observations, we have included in our analysis only pixels with Lyα and metal optical depth higher than 10^{-3}.

Comparison with the filament environment

As we have discussed, the target galaxy and its wind bubble are embedded in a cosmic filament essentially aligned perpendicular to the plane of the maps shown in Fig. 1. In order to investigate the spectral differences between the wind and the filament environments, we have compared LOSs passing through the wind bubble and those intersecting the filament. Both Pixel Optical Depth (Fig. 5) and Voigt profile fitting (Fig. 6) analysis give inconclusive results. We find then very difficult to discriminate cosmic web structures from those created by the galactic wind purely from available absorption data. The main reason is that cold clumps resulting from the fragmentation of the supernova-driven shell have properties that hardly differ from those of the filament hosting the system. Most of the absorption systems will arise from these dense structures rather than from the hot, rarefied interior.

Target galaxy

To identify a suitable representative target galaxy in the simulation box showinga strong wind, we have searched in the high-resolution run output at z=3.26 for high density (n > 10^{-2} cm^{-3}), high temperature (T > 10^6 K) and high peculiar velocity particles. The total mass of the selected target galaxy which fulfills the above listed conditions is ~10^{11} $M_\odot$, i.e. a mass typical for Lyman Break Galaxies (LBG). In Fig. 2 we show 2D maps of different quantities in a plane across the target galaxy center. The signature of the wind is clearly seen as a region of enhanced temperature in the corresponding map. The shock caused by the outflow has heated up the gas to a temperature ~10^6 K (wind bubble), but the outflowing gas is being slowed down by the infalling material (see the low pressure arc to the left of the bubble). The spatial distribution of the metallicity (lower panels) is very similar to the temperature, clearly indicating that the bubble has been created by supernova explosions within the target galaxy. However, the presence of PopIII-enriched cold clumps falling toward the galaxy (upper portion of the map) could require a previous star formation activity which pollutes the streams. In summary, the galactic region is characterized by two different environments: (i) the filament in which the galaxy is embedded, and (ii) the wind environment, in turn constituted by the wind bubble, infalling streams and cold clumps accreting onto the galaxy.

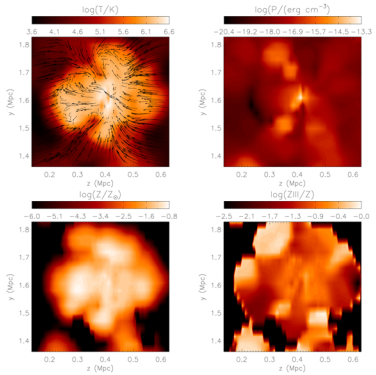

Figure 2. Maps of various quantities across the target galaxy center. *Upper left*: temperature and peculiar velocity field (arrows; the largest one corresponds to 250 km s-1); *Upper right*: ram-pressure; *Bottom left*: total metallicity; *Bottom right*: PopIII-to-total metallicity ratio. Sizes are in physical units.

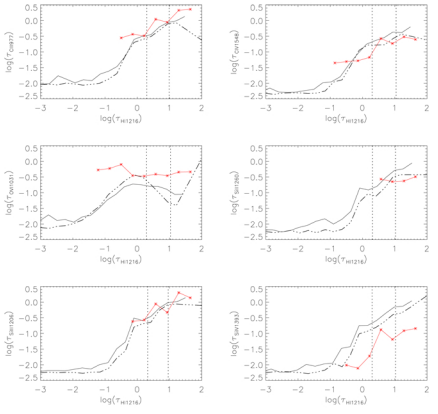

Figure 5. Pixel Optical Depth analysis results for the synthetic spectra. Plotted are the optical depths of various low- high-ionization species against the HI Lyα optical depth in the filament (solid lines) and in the wind (dashed-dot) environment; the starred line represents observational data from the VLT/UVES LP. The two vertical lines mark the points at which Lyα (leftmost) or Lyβ (rightmost) absorption reaches 85% of the continuum level. Only bins with more than 50 data points are shown.

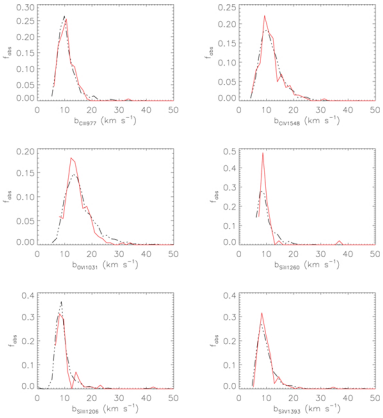

Figure 6. Simulated Doppler parameter distribution for the different ions. Dotted (solid) lines refer to the filament (bubble) environment.

Alternative strategies

As pointed out before, the bubble environment is characterized by log T > 5.5 and highly ionized species such as OVI, OVII and OVIII (Fig. 3). Among these ions, only the OVI transition falls within the UVES wavelength range, while those of OVII (λ=21.6 Å) and OVIII (18.97 Å) are located in the X-ray band. It is then interesting to briefly outline the general trends of the optical depth distribution also for these species. The optical depth for each transition has been computed using the *in situ* approximation. To check its sensitivity to temperature, as a test we have fixed the density to the typical values found in the bubble and in cool/filament regions, that is log<n> ~ -3.7 and log<n> ~ -2.7, respectively. In Fig. 7 we show the predicted OVII/OVIII optical depths (normalized to the corresponding OVI one) as a function of temperature for both environments. Both OVIII and OVII are expected to provide larger opacities at high temperatures (log T > 5.5) with respect to OVI, implying that these species would be particularly well suited to study the hot component of high redshift galactic winds.

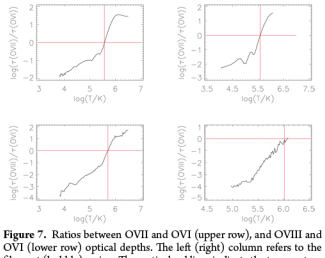

Figure 7. Ratios between OVII and OVI (upper row), and OVIII and OVI (lower row) optical depths. The left (right) column refers to the filament (bubble) region. The vertical red lines indicate the temperature where the two optical depth become equal.

References

Aguirre A., Dow-Hygelund C., Schaye J., Theuns T.: 2007, arXiv0712.1239A
Aguirre A., Schaye J., Kim T., Theuns T., Rauch M., Sargent W.L.W.: 2004, ApJ, 602, 38A
Haardt F. & Madau P.: 2001, cghr.confE, 64H
Marri S. & White S.D.M.: 2003, MNRAS, 345, 561
Schaye J., Aguirre A., Kim T.-S., Theuns T., Rauch M. and Sargent W.L.W.: 2003, ApJ, 596, 768
Schneider R., Ferrara A., Natarajan P., Omukai K.: 2002ApJ, 571, 30S
Simcoe R.A., Sargent W.L.W., Rauch M.: 2004, ApJ, 606, 92S
Telfer R.C., Kriss G.A., Zheng W., Davidsen A.F., Tytler D.: 2002, ApJ, 579, 500T
Springel V., Yoshida N. & White S.D.M.: 2001, ApJ, 546, 665

**fangano@astro.uni-bonn.de*